geosciences

MDPI

Article

Mantle Xenoliths from Huanul Volcano (Central-West Argentina): A Poorly Depleted Mantle Source under Southern Payenia

Gustavo W. Bertotto [1], Maurizio Mazzucchelli [2,*], Tommaso Giovanardi [2,*], Rommulo V. Conceiçao [3], Alberto Zanetti [4], Manuel E. Schilling [5], Mauro I. Bernardi [1], Alexis D. Ponce [1], Tiago Jalowitzki [6], Fernanda Gervasoni [7] and Anna Cipriani [2,8]

[1] INCITAP, CONICET-Universidad Nacional de La Pampa, Santa Rosa 6300, Argentina; gwbertotto@yahoo.com.ar (G.W.B.); mi_bernardi@hotmail.com (M.I.B.); poncealexis_wini@hotmail.com (A.D.P.)
[2] Dipartimento di Scienze Chimiche e Geologiche, Università di Modena e Reggio Emilia, I-41125 Modena, Italy; anna.cipriani@unimore.it
[3] Instituto de Geociências, Universidade Federal do Rio Grande do Sul (UFRGS), Porto Alegre 91501970, Brazil; rommulo.conceicao@ufrgs.br
[4] Consiglio Nazionale per le Ricerche, I-27100 Pavia, Italy; zanetti@crystal.unipv.it
[5] Instituto de Ciencias de la Tierra, Facultad de Ciencias, Universidad Austral de Chile, Valdivia 5090000, Chile; manuel.schilling@uach.cl
[6] Instituto de Geociências, Universidade de Brasília (UnB), Brasília 70910-900, Brazil; jalowitzki@unb.br
[7] Faculdade de Ciências e Tecnologia, Universidade Federal de Goiás (UFG), Goiânia 74968-755, Brazil; gervasoni.fe@gmail.com
[8] Lamont-Doherty Earth Observatory, Columbia University, 61 Route 9W, Palisades, NY 10964, USA
* Correspondence: maurizio.mazzucchelli@unimore.it (M.M.); tommaso.giovanardi@unimore.it (T.G.)

Citation: Bertotto, G.W.; Mazzucchelli, M.; Giovanardi, T.; Conceiçao, R.V.; Zanetti, A.; Schilling, M.E.; Bernardi, M.I.; Ponce, A.D.; Jalowitzki, T.; Gervasoni, F.; et al. Mantle Xenoliths from Huanul Volcano (Central-West Argentina): A Poorly Depleted Mantle Source under Southern Payenia. *Geosciences* **2022**, *12*, 157. https://doi.org/10.3390/geosciences12040157

Academic Editors: Roberto Moretti and Jesus Martinez-Frias

Received: 5 March 2022
Accepted: 29 March 2022
Published: 1 April 2022

Abstract: Huanul is a shield volcano with several lava flows hosting mantle xenoliths erupted during the Pleistocene (0.84 ± 0.05 Ma). It is located in the southern part of the Payenia Volcanic Province, which is among the largest Neogene-Quaternary volcanic provinces of South America. The volcanism here has been ascribed as the northernmost expression of the back-arc volcanism of the Andean Southern Volcanic Zone. We present the first petrographic and mineral chemistry study of mantle xenoliths collected from Huanul lavas with the aim of reconstructing directly the mantle source of the Payenia Volcanic Province. Xenoliths are commonly small (<5 cm in radius) but scarcely crossed by basaltic veins. All xenoliths have a fertile lherzolitic modal composition and are equilibrated in the spinel-facies. Most of them exhibit an almost primitive-mantle geochemical affinity, characterized by slightly depleted clinopyroxene REE patterns reproducible by partial melting degrees between 0 and 4% of a PM source. Geothermobarometric P-T estimates of clinopyroxene-orthopyroxene couples form a linear trend between 10 and 24 kbar with constant increase of T from 814 to 1170 °C along a 50–60 mW/m^2 geotherm. Evidences of interaction with the host basalts occur as spongy textures in clinopyroxene and reacted spinel, which tend to became more restitic in composition and show chromatographic or complete overprinting of the trace element compositions. The presence of plagioclase and calculated P-T values constrain this melt/rock reaction process between 6 and 14 kbar, during magma ascent, and fit the mantle adiabat model. Calculated melts in equilibrium with the primary clinopyroxenes do not fit the composition of the host basalt and, together with the geothermobarometric estimations, point to an asthenospheric mantle source for the magmatism in southern Payenia. The PM geochemical affinity of the xenoliths of Huanul is an extremely rare finding in the South America lithospheric mantle, which is commonly extensively refertilized by subduction-derived melts.

Keywords: Huanul; Payenia; Patagonia; mantle xenoliths; mantle wedge

1. Introduction

The territories of South America located south of 33 °S are famous for the occurrence of mantle xenoliths within basaltic lavas and pyroclastic structures. Many of these volcanic fields and xenoliths have been recognized and investigated in the last two decades increasing our knowledge on the general characteristics of the subcontinental lithospheric mantle (SCLM), as well as the detailed structure of the mantle column at several localities (e.g., [1–15]). A complicating factor in the study of these mantle xenoliths is the development of the Pacific subduction, currently represented by the Nazca and Antarctic oceanic plates, below the South American continent. This process has profoundly influenced at many locations the chemistry of the subcontinental mantle up to ca. 700 km of distance from the Chilean trench, due to the introduction of slab-derived components along the back-arc region. Therefore, over time, volcanism and subduction have contributed in several episodes to the depletion, metasomatism and refertilization of the SCLM, and the results of these processes are commonly archived by mantle xenoliths transported to the surface by the Tertiary-Quaternary magmas. According to various studies, multiple events of metasomatism, depletion and refertilization are widely recorded by xenoliths from the entire Patagonia, and only very rarely are xenoliths here representative of a primary primitive SCLM (e.g., [7,9,11–14,16–19] and references therein).

In this paper, we present mineral chemistry data of the first occurrence of xenoliths located in the Southern Payenia Volcanic Province (Mendoza province, Argentina), where it was recently proposed, through a study of the lavas, that the mantle source has been affected by refertilization processes [20]. Xenoliths were collected from lava flows of the Huanul shield volcano. Mineral phases were analysed for major (olivine, orthopyroxene, clinopyroxene, and spinel) and trace elements (clinopyroxene). We aim to reconstruct the chemical and geothermobarometric features of the Huanul mantle column prior to the xenoliths' ascent and prior to the interaction with the alkaline melts transporting media.

2. Geological Setting

The Huanul volcano is located in the southern part of the Payenia Volcanic Province (hereafter Payenia), at 37°17′ S and 68°32′ W, about 480 km east of the Chilean trench in the Mendoza province (Figure 1).

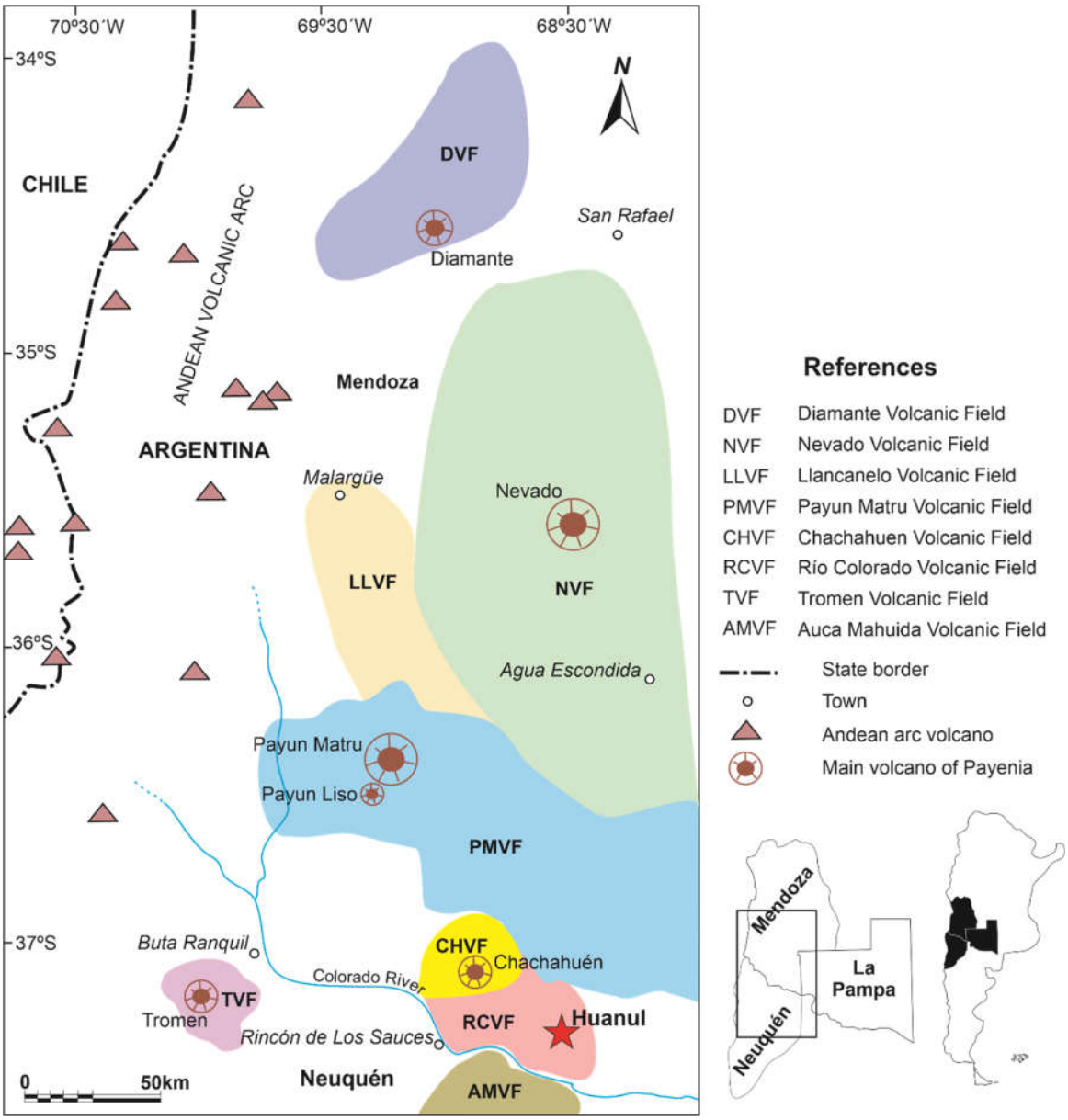

Figure 1. Geological sketch map of the Payenia Volcanic Field showing the Huanul volcano, modified from Bernardi et al. [21].

The Cenozoic magmatism that formed this province affected the central-western region of Argentina and produced volcanic fields in Mendoza, La Pampa, and Neuquén provinces. This igneous activity was almost continuous from the Miocene to the Holocene and mainly formed a wide basaltic plateau that covers the extra-Andean back-arc [21–28]. A gap in the volcanic activity related to regional geodynamics has been identified between the late Miocene and the early Pliocene. Here the stress regime has changed from compressive during Miocene [29,30] to extensional in the Pliocene–Holocene [23,28,30]. This change and the migration of the volcanic activity toward the west were likely controlled by the steepening of the subducted Nazca plate that led to the ascent of the asthenosphere [29,31–34].

Payenia is located between 460 to 540 km east of the Chile Trench and comprises the largest Neogene-Quaternary volcanic province of South America. The volcanism is manifested as numerous basaltic cinder cones, few andesitic-dacitic composite volcanoes,

and lava flows, several of which are extraordinarily long, up to 180 km (e.g., [25,35–37]). Its southern part is occupied by a small volcanic field named Río Colorado Volcanic Field [25,28,37–39] constituted by pahoehoe lava flows in a northwest–southeast direction. Here, the most important eruptive center is Huanul, a shield volcano (Figure 2) built from basaltic lava flows and pyroclastic aggregates. Its crater is 4 km in diameter and rises ca. 20 m from the surrounding [21]. The basaltic flows overlay the sedimentary rocks of the Neuquén Basin (Jurassic to Paleogene) and the Quaternary sediments of the Colorado river. Eight lava units are currently recognized in the field, and the oldest one, named El Corcovo lava flow, covers a distance of ca. 70 km for an area of ca. 415 km^2 [21]. El Corcovo consists of alkaline basalts with a K-Ar age of 0.84 ± 0.05 Ma [40].

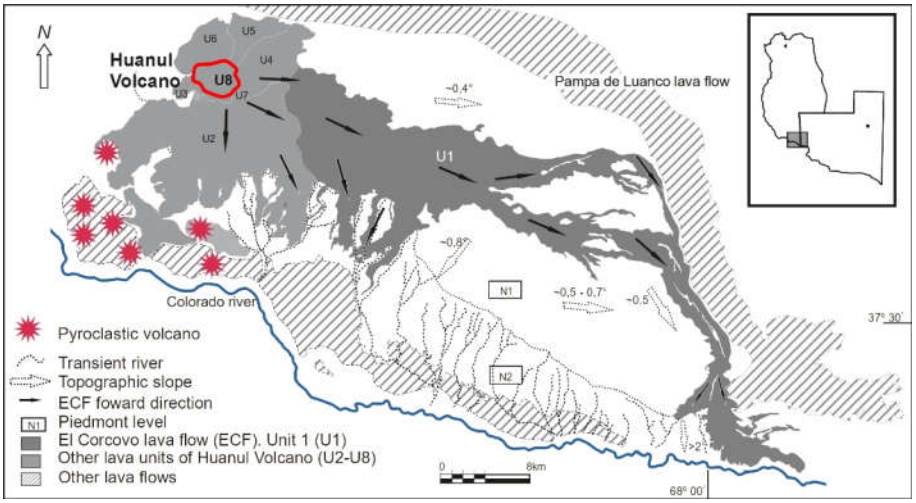

Figure 2. Local geological setting and topographic features of the lava flows of Huanul volcano and surrounding area of the Rio Colorado Volcanic Field modified after Bernardi et al. [21]. The xenoliths were collected from Unit 8 in the red-circled area. ECF: El Corcovo Lava flow.

Detailed information on the Huanul volcanism and eruption types are reported by [28,35,41,42]. Here, we summarize the characteristics of the Huanul lava flow from which our xenoliths were collected. They are porphyric basalts with holocrystalline, intergranular and felted groundmass, and subordinate subophitic and intersertal microtextures. The latter is more frequent in the superficial layer of the lava flow. Phenocrysts are mainly olivine and plagioclase (15 to 30%) and minor clinopyroxene (<2%). Olivine is on average 1.2 mm in size (up to 2.5 mm). It commonly exhibits subhedral to euhedral shapes, with short columnar habits with well-developed pseudohexagonal and hexagonal sections that include equidimensional opaque minerals of the spinel group. It is partially alterated to low temperature iddingsite (IBT) at the edges and fractures, and sometimes the central sectors develop high temperature iddingsite (IAT). The plagioclase phenocrysts are subhedral, mainly aligned along the flux direction, and with maximum sizes up to 6 mm, mainly around 1 to 2.5 mm. Clinopyroxene phenocrysts and microphenocrysts are characterized by subhedral morphologies and columnar to prismatic habits, up to 1.5 mm and on average 0.6 mm in size.

Glomerular phenocrysts show the following mineralogical associations: (1) plagioclase; (2) plagioclase-olivine; (3) plagioclase-olivine-clinopyroxene and (4) plagioclase-clinopyroxene. The groundmass generally is composed by microliths of subhedral plagioclase and anhedral and interstitial clinopyroxene. Locally, ehuedral to subhedral olivine is associated with opaque minerals with polyhedral to anhedral equant and prismatic habits.

The geochemical data of the host lava were reported by [41] with compositions in the range of variability of ocean island basalts (OIB) and transitional basalt of Patagonia [43].

3. Analytical Methods

Nineteen xenoliths were collected for petrographic and geochemical investigations. Thirteen samples were selected for major element analyses of the mineral phases. Among them, ten samples were selected for trace elements analyses on clinopyroxene.

Major elements of the main mineral phases (olivine, orthopyroxene, clinopyroxene, and spinel) were determined at the Dipartimento di Scienze della Terra of the Università di Milano (Italy) by a JEOL JXA-8200 electron microprobe with 15 kV accelerating voltage, 15 nA beam current, 1–3 μm beam diameter, 30 s counting time on the peaks and 10 s on the background. Natural minerals (olivine for Mg; omphacite for Na; ilmenite for Ti; rodonite for Mn; K-feldspar for K; anorthite for Al and Ca; wollastonite for Si; fayalite for Fe, and nicolite for Ni) and synthetic chromite for Cr were used as standards. The results were corrected for matrix effects using the conventional ZAF method provided by the JEOL suite of programs. Results are considered to be accurate within 2–6%. Details on the method are reported in [44]. Data are presented in the Supplementary Materials Table S1.

Trace elements spot analyses on the selected clinopyroxene samples were determined by Laser Ablation-Inductively Coupled Plasma Mass Spectrometry (LA-ICP-MS), using a Thermo Fisher Scientific mass spectrometer coupled to a laser ablation New Wave UP 213 at the Laboratory of the Centro Interdipartimentale Grandi Strumenti (CIGS) of the Università di Modena e Reggio Emilia. Detailed method is reported in [45]. Data reduction was performed with the Thermo Fisher Scientific PlasmaLab® software using NIST610, NIST612 and NIST614 as external standards. The isotope ^{44}Ca was used as internal standard for clinopyroxene. Laser spot size was calibrated at 50 μm and laser beam fluency at 20 microJoule for cm^2. Data are reported in the Supplementary Materials Table S2.

4. Results

4.1. Petrography

The Huanul xenoliths are small, commonly smaller than 5 cm, and rounded. The modal composition of the nineteen samples indicates that all samples are lherzolite equilibrated in the spinel-facies (Figure 3a; Table 1).

Table 1. Modal compositions of Huanul xenoliths.

Sample	Classification	Texture	% Ol	% Opx	% Cpx	% Sp	% Veins
HU2	spinel-bearing lherzolite	Mosaic-porphyroclastic	62.45	20.02	14.47	3.06	0.00
HU11	spinel-bearing lherzolite	Porphyroclastic	68.21	13.79	10.48	4.45	3.08
HU12	spinel-bearing lherzolite	Porphyroclastic	56.10	12.91	21.93	3.48	5.58
HU13	spinel-bearing lherzolite	Granuloblastic	61.39	9.98	17.10	2.09	9.45
HU14	spinel-bearing lherzolite	Granuloblastic	67.23	19.77	7.93	2.37	2.70
HU15	spinel-bearing lherzolite	Mosaic-porphyroclastic	84	5.27	7.06	2.09	1.09
HU17	spinel-bearing lherzolite	Porphyroclastic	66.04	22.13	9.20	2.63	0.00
HU19	spinel-bearing lherzolite	Mosaic-porphyroclastic	50.55	32.77	12.47	2.73	1.48
HU20	spinel-bearing lherzolite	Mosaic-porphyroclastic	63.41	14.56	17.37	2.04	2.62
HU21	spinel-bearing lherzolite	Porphyroclastic	55.96	23.84	13.14	2.93	4.12

HU22	spinel-bearing lherzolite	Porphyroclastic	47	29.21	15.74	3.95	4.40
HU23	spinel-bearing lherzolite	Porphyroclastic	83.47	5.49	6.13	0.38	4.53
HU25	spinel-bearing lherzolite	Granuloblastic	66.96	21.96	6.03	1.84	3.22
HU30	spinel-bearing lherzolite	Mosaic-porphyroclastic	55.3	26.2	11.1	4.4	3.1
HU32	spinel-bearing lherzolite	Mosaic-porphyroclastic	51.77	32.31	12.23	2.67	1.02
HU33	spinel-bearing lherzolite	Porphyroclastic	57.47	21.55	16.87	2.91	1.20
HU34	spinel-bearing lherzolite	Porphyroclastic	54.69	26.43	12.37	2.93	3.59

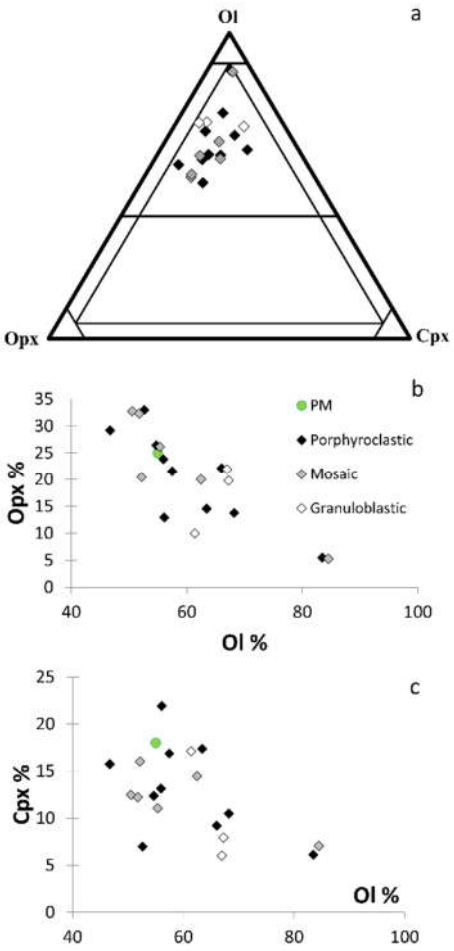

Figure 3. (**a**) Modal classification of Huanul mantle xenoliths showing that our samples have lherzolitic composition. Modal compositions were estimated by point counting (minimum 1200 points for sample). (**b**) Orthopyroxene and (**c**) clinopyroxene versus olivine content in the Huanul lherzolitic xenoliths.

Textures after [46] vary from porphyroclastic (10 samples) to mosaic-porphyroclastic (6 samples) to granuloblastic (3 samples) (Figure 4A–D).

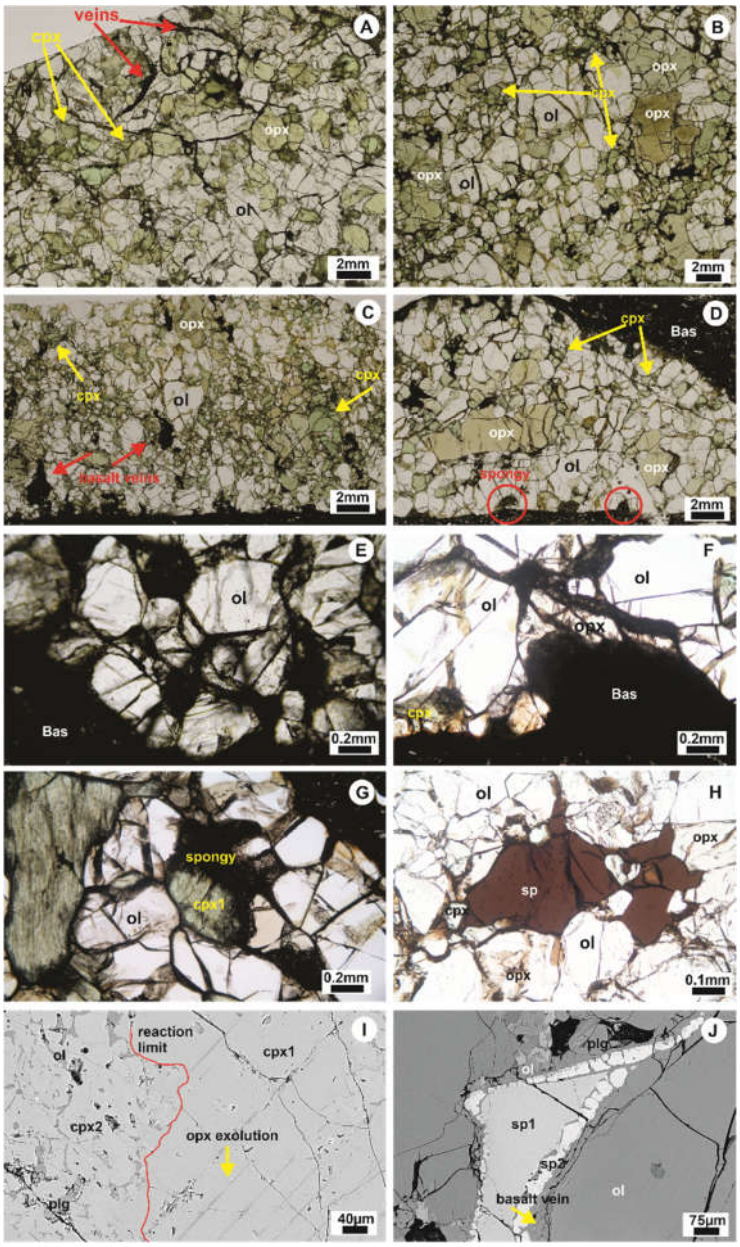

Figure 4. Petrographic features of Huanul xenoliths showing the main mineral phases and textures. ol = olivine, opx = orthopyroxene, cpx = clinopyroxene, sp = spinel, bas = host basalt. (**A**) granuloblastic texture, sample HU14; (**B**) porphyroclastic texture, sample HU34; (**C**) mosaic-porphyroclastic texture sample HU32; (**D**) porphyroclastic texture, sample HU17; (**E**) neoblasts in sample HU15; (**F**) orthopyroxene dissolution at the host basalt contact in sample HU23; (**G**) spongy texture around a primary clinopyroxene in sample HU12; (**H**) aggregate of primary spinels, sample HU32; (**I**) detail of the spongy-primary clinopyroxene contact, sample HU12; (**J**) reaction rims of spinel in contact with a basalt vein, sample HU25.

No correlation is recognized between modal composition and texture (Figure 3).

Basaltic veins are present in most of the xenoliths in percentages varying from 1.02 to 9.45 Vol.% (Table 1) with only two samples being vein-free. Veins are thin, only few µm thick, and develop at the borders with minerals (Figure 4A). We commonly recognize their shapes up to the contact with the host basalt. Similar to the host basalt, basaltic veins are holocrystalline and formed by a groundmass with association of olivine±plagioclase±clinopyroxene in variable abundances. Olivine at the contact with the

vein does not show any change while orthopyroxene, clinopyroxene and spinel tend to form reaction structures. Two populations of olivine are commonly observed. The larger olivines (of ca. 4–5 mm) are anhedral and show kink-bands. Smaller, recrystallized olivine grains (0.5–2 mm) do not have kink-bands and develop triple junctions. Orthopyroxene is anhedral with maximum length, ranging from 2 to 8 mm. Commonly, it develops exsolution lamellae of clinopyroxene, but, when in contact with the hosting lava, it shows resorption rims with disappearance of exsolution lamellae and formation of lobate shapes (Figure 4D), thus evidencing dissolution features (Figure 4F). Clinopyroxene has maximum width ranging between 1.5 and 3.5 mm, is anhedral and exhibits exsolution lamellae of orthopyroxene. When in contact with basaltic veins or the host basalt, clinopyroxene tends to assume a spongy texture, with formation of new, un-exsolved, pecilitic clinopyroxene with inclusions of olivine and plagioclase (Figure 4G,I). This recrystallization is either complete or partial, with cores commonly characterized by exsolution lamellae and spongy rims. Not all samples show this feature, which depends on the presence of basaltic veins in contact with clinopyroxene. Two samples are characterized only by spongy clinopyroxene: mosaic sample HU14, where clinopyroxenes are almost completely spongified, and porphyroclastic sample HU15, where clinopyroxene cores are surrounded by spongy domains.

Spinel is interstitial, up to 2 mm, anhedral, and frequently holly leaf shaped. It is brown in color and can form crystal aggregates (Figure 4H). Similar to clinopyroxene, spinels show reaction textures with the formation of spinel-2 coronas in a matrix of olivine and plagioclase when in contact with basaltic veins (Figure 4I).

4.2. Mineral Phases Major Elements

The Mg# content (calculated as Mg# = $[Mg^{2+}/(Mg^{2+} + Fe^{2+}_{tot})] \times 100$ mol.) of olivine porphyroclasts varies between 88.9 and 90.5. No geochemical differences could be recognized among the different textures (i.e., porphyroclastic, mosaic and granuloblastic; Figure 5).

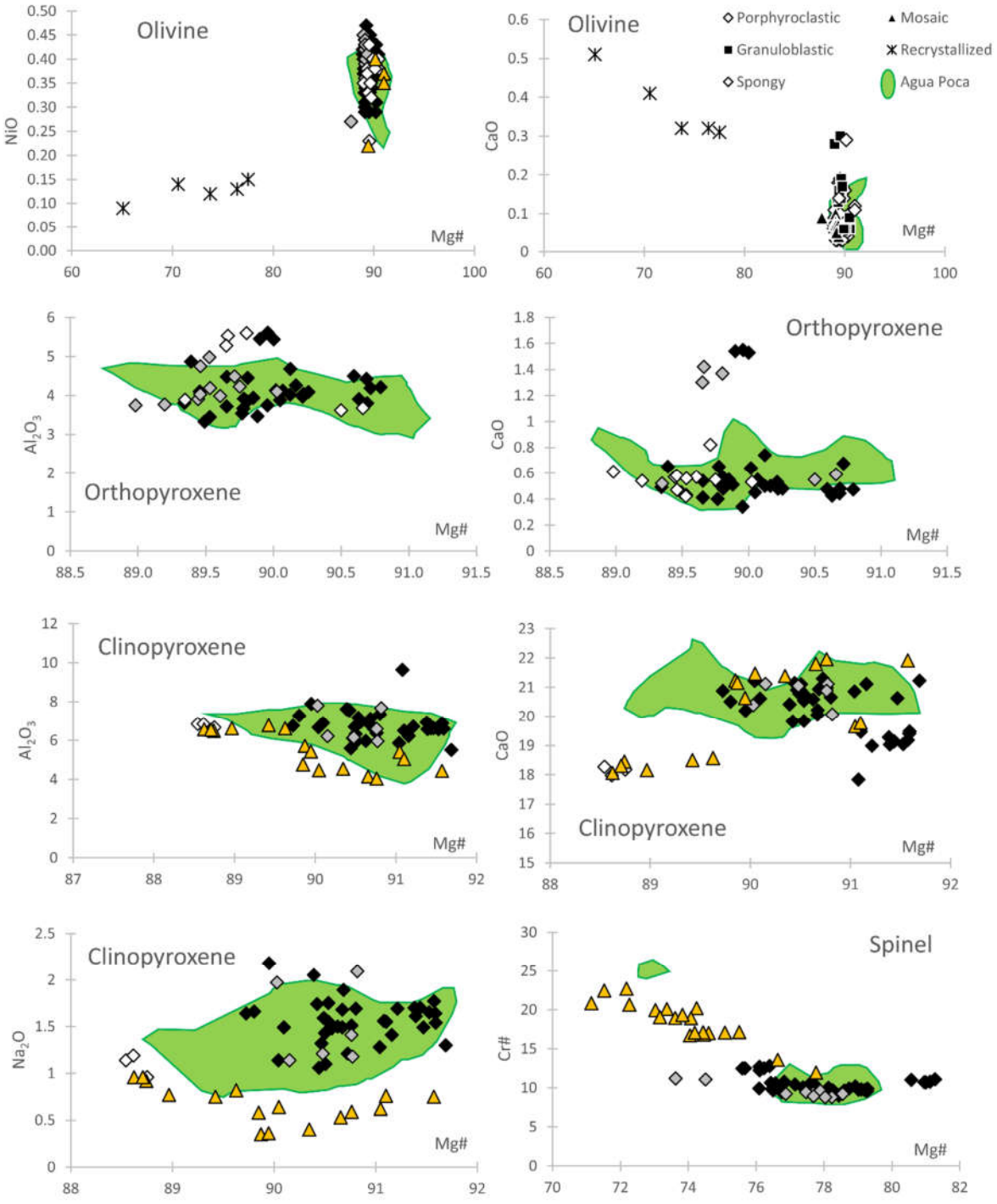

Figure 5. Major element variations in olivine, orthopyroxene, clinopyroxene and spinel from Huanul xenoliths. Green fields are major elements variations of Agua Poca xenoliths [10].

Neoblasts in a mosaic-recrystallized zone of sample HU15 have lower Mg# values (from77.5 to 65.1) and SiO_2 (36.84–38.51 wt.%) compared to other olivines (40.35–40.90 wt.% r). An olivine crystal in contact with the reaction zone shows Mg# of 87.7 (Figure 5. The olivine neoblasts are depleted in NiO (0.09–0.15 wt.%), in MnO (0.30–0.49 wt.%) and in CaO (0.31–0.51 wt.%) compared to the porphyroclasts (Supplementary Materials Table

S1). Olivine from spongy domains of clinopyroxene and reacted spinel has Mg# of 89.4–91.0, MnO between 0.14–0.28 wt.%, NiO between 0.22–0.40 wt.% and CaO between 0.11–0.29 wt.%.

Orthopyroxene has Mg# between 89.0 and 90.7 (Figure 5). In general, CaO is between 0.34–0.98 wt.% with the exceptions of one mosaic sample (HU14, CaO = 0.52–1.42 wt.%) and a porphyroclastic one (sample HU23, CaO = 1.53–1.55 wt.%) (Supplementary Materials Table S1). Al_2O_3 is mainly between 3.33 and 4.98 wt.% with the exception of orthopyroxene from sample HU14 (3.89–5.6 wt.%) and HU23 (5.44–5.61 wt.%) (Figure 5).

Clinopyroxene Mg# varies between 89.7 and 91.7, while one granuloblastic sample (HU14) has lower Mg# between 88.5–88.8 (Figure 5). The majority of the samples shows Al_2O_3 between 5.51 and 7.89 wt.%, but one is up to 9.64 wt.% (Supplementary Materials Table S1). CaO varies between 17.84–21.30 wt.%, and Na_2O is between 1.06–2.18 wt.%. Clinopyroxene from granuloblastic sample HU14 shows higher Cr_2O_3 (1.07–1.16 and 0.56–1.08 wt.%, respectively) but abundances of Al, Ca and Na comparable to the other clinopyroxenes (Supplementary Materials Table S1). Spongy clinopyroxenes have Mg# (88.6–91.6) and CaO (18.06–21.96 wt.%) within the range of primary clinopyroxenes, but they are depleted in Al_2O_3 (4.04–6.78 wt.%) and Na_2O (0.35–0.96 wt.%).

Spinel has Mg# between 73.6–81.3 and Cr# (calculated as Cr# = $[Cr^{3+}/(Cr^{3+} + Al^{3+})] \times 100$ mol.) between 8.8 and 12.8. Reacted spinels form an inverse trend for Mg# and Cr# (Figure 5) showing higher Cr# (11.9–22.7) and lower Mg# (71.1–77.8) compared to primary spinels. In reacted textures, spinels from the corona are commonly more enriched in Cr# (e.g., sample HU25, 22.5–22.7) and lower in Mg# (71.5–72.2) than the core (17.0–17.1 and 74.2–75.5).

4.3. Clinopyroxene Trace Elements

The trace elements composition of Huanul clinopyroxenes is very homogeneous within sample. Thus, in the diagrams, we use average values (Table 2) as representative of each sample. The complete dataset is reported in Supplementary Materials Table S2.

Clinopyroxene REE patterns are mainly depleted in LREE and flat-like in M- and H-REE (Figure 6).

Table 2. Average trace elements composition of Huanul clinopyroxenes. Values are reported in ppm.

Sample	HU11	HU12	HU14	HU15	HU19	HU20	HU21	HU32	HU33	HU34
Sc	63	59	42	50	63	64	63	62	60	62
Ti	2965	2741	2285	1563	2221	3304	2261	3388	3240	2712
V	180	186	120	163	186	234	226	246	239	226
Cr	6132	5645	7541	2999	5684	5502	5694	5153	5803	5324
Rb	0.465	0.050	1.02	0.176	0.060	0.217	0.047	0.011	0.007	0.008
Sr	52	37	114	103	29	58	33	33	48	38
Y	16	17	14	10	16	17	14	18	17	16
Zr	35	27	29	20	24	34	25	24	27	26
Nb	0.030	0.009	0.234	0.033	0.004	0.090	0.007	0.003	0.007	0.003
Cs	0.021	0.008	0.043	0.022	0.018	0.033	0.039	0.009	0.007	0.008
Ba	245	0.356	70	1.49	0.086	279	0.234	0.131	0.082	0.021
La	0.820	0.473	2.99	2.11	0.348	1.06	0.505	0.269	0.561	0.476
Ce	3.5	2.13	10	3.2	2.03	3.3	1.80	1.75	2.40	2.09
Pr	0.677	0.469	1.48	0.439	0.467	0.576	0.364	0.440	0.510	0.435
Nd	4.4	3.6	8.6	3.0	3.6	4.23	3.0	3.8	4.0	3.6
Sm	1.56	1.74	2.45	1.19	1.56	1.89	1.44	1.80	1.85	1.67
Eu	0.617	0.689	0.873	0.496	0.646	0.721	0.573	0.723	0.750	0.656
Gd	2.29	2.48	2.70	1.59	2.35	2.66	2.16	2.68	2.59	2.38
Tb	0.428	0.452	0.424	0.276	0.423	0.462	0.386	0.463	0.442	0.426
Dy	3.0	3.2	2.78	2.02	2.97	3.4	2.85	3.4	3.3	3.1
Ho	0.642	0.682	0.583	0.430	0.639	0.702	0.596	0.722	0.693	0.636

Er	1.92	2.03	1.58	1.29	1.92	2.14	1.82	2.21	2.13	2.02
Tm	0.274	0.282	0.201	0.167	0.282	0.292	0.251	0.294	0.289	0.276
Yb	1.89	1.91	1.32	1.18	1.87	2.10	1.79	2.18	2.08	2.01
Lu	0.257	0.253	0.167	0.162	0.250	0.254	0.228	0.274	0.265	0.262
Hf	0.933	0.966	0.975	0.774	0.965	1.13	0.851	0.946	0.953	0.924
Ta	0.002	0.002	0.020	0.006		0.005	0.002	0.001	0.002	0.001
Pb	0.153	0.044	0.031	0.100		0.215	0.028	0.048	0.063	0.052
Th	0.042	0.005	0.024	0.194	0.003	0.016	0.013	0.001	0.001	0.002
U	0.021	0.002	0.010	0.059	0.003	0.007	0.008	0.003	0.003	0.001

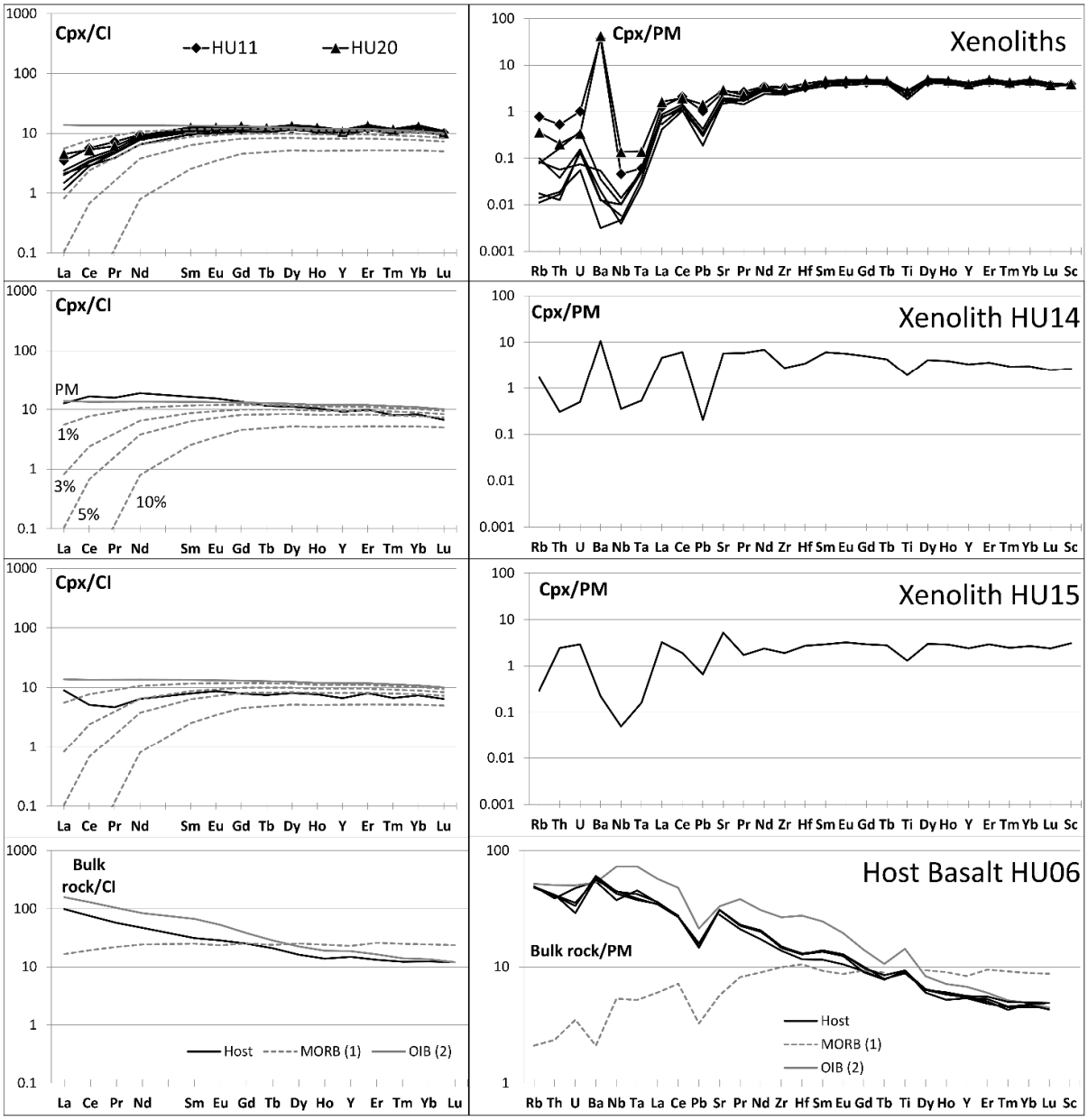

Figure 6. REE and trace elements spiderdiagrams of clinopyroxenes from Huanul mantle xenoliths and host basalt (sample HU06 from Bertotto et al. [41]). REE patterns are normalized to Chondrite-I values (CI) of Lyubetskaya and Korenaga [47]. Spiderdiagrams are normalized to the Primite Mantle (PM) values of McDonough and Sun [48]. The pattern of a primitive mantle-clinopyroxene (solid grey line) of Sun and McDonough [49] and patterns (dotted gray lines) after 1, 3, 5, and 10%

of depletion by partial nonmodal melting are also shown. Pattern of MORB [50] and OIB [49] are reported for comparison.

These patterns are similar to those of clinopyroxenes produced by low degree of partial melting of a PM source (up to 3%), calculated from the composition of a PM [50] using the partition coefficients of Ionov et al. [51] for a spinel-facies mantle peridotite. The LILE and HSFE abundances of these clinopyroxenes are low with negative anomalies of Pb, Ti, Ba and Nb (Figure 6).

The porphyroclastic cores with spongy rims of HU15 clinopyroxenes are characterized by almost flat M- to H-REE patterns with enrichments in La and Ce. These patterns from Lu to Eu follow closely those of a clinopyroxene derived from a PM source after 5% of partial melting (Figure 6). The extended trace elements pattern is somewhat similar to the other porphyroclastic clinopyroxenes but with positive anomalies for U, Th and Sr.

The HU14 spongified clinopyroxene shows a convex-upward REE pattern (Figure 6). Its extended trace element pattern is more enriched compared to porphyroclastic clinopyroxenes (Figure 6) and shows a strong positive Ba anomaly and a negative Pb and moderately negative Zr-Hf anomalies.

4.4. Geothermobarometry

Pressure (P) and temperature (T) were calculated for primary pyroxenes using clinopyroxene-only and clinopyroxene–orthopyroxene exchange geothermobarometers ([52–56], Table 1).

An extensive discussion about the precision and accuracy of the geothermometers used in Table 1 is reported in [56,57]. According to the latter, the best P estimates for spinel-facies peridotites can be obtained with the geobarometer of [53]. The P values calculated for Huanul using equations of [53] were then used to estimate T, according to each thermometer. We discuss the T data of primary pyroxenes using the two-pyroxenes geothermometer of Brey and Köhler [54] because it is the most suitable for peridotite xenoliths in spinel-facies ([56]) and is widely used in the literature for Patagonia mantle xenoliths (e.g., [4,10,11]). We are using instead the geothermobarometer equations of Wang et al. [58] to discuss spongy clinopyroxene because these equations are an implementation of those of Putirka [59] and are suitable for samples equilibrated in the plagioclase facies. The estimated T obtained by different geothermometers are in good agreement, showing parallel trends and almost constant difference in values (Table 3).

Primary pyroxenes show almost linear trends from 25 to 10 kbar (Figure 7; Table 3).

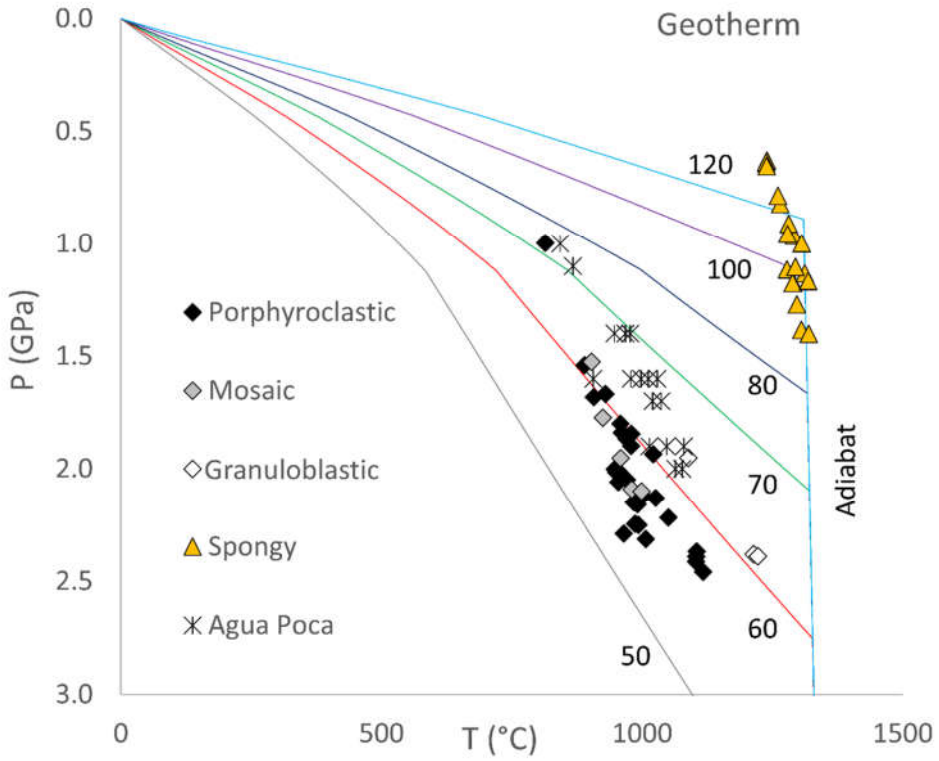

Figure 7. Pressure (GPa) vs. Temperature (°C). Temperatures were calculated with the two-pyroxenes geothermometer of Brey and Köhler [54] for primary pyroxenes and with equations of Wang et al. [58] for spongy clinopyroxenes. Pressure was calculated with the clinopyroxene geobarometer of Mercier [53] for primary pyroxenes and with equations of Wang et al. [58] for spongy clinopyroxenes. For comparison, available data of mantle xenoliths from Agua Poca [10] were plotted together with geotherms calculated with the equations of Hasterok and Chapman [60] from 50 to 120 mW/m^2.

Porphyroclastic and mosaic textured samples form a unique trend, while cores of spongy clinopyroxenes from granuloblastic sample HU14 form a parallel trend at higher T. Temperature estimates for mosaic and porphyroclastic samples range between 814 and 1117 °C, while granuloblastic sample HU14 varies between 1089 and 1222 °C (Figure 7; Table 3). It is interesting to note that xenoliths from the Agua Poca volcano show a geotherm trend higher than Huanul samples and comparable to the trend of the granuloblastic sample HU14 (Figure 7). Comparing Huanul xenoliths T-P estimations with the geotherm calculated with the equations of Hasterok and Chapman [60] based on surface heat estimations, mosaic and porphyroclastic samples show a steeper trend between 50 and 60 mW/m^2, while granuloblastic and Agua Poca samples are comprised between 60 and 70 mW/m^2 (Figure 7).

Spongy clinopyroxenes show a higher geotherm at lower P compared to primary pyroxenes and Agua Poca (Figure 7). Although the equations of Wang et al. [58] are fitted for P between 0–12 kbar, the good agreement of values up to 14 kbar (better than values obtained from Putirka, [59] Table 3) suggests that these values are not meaningless. Spongy clinopyroxene estimates range between 6.3 and 14 kbar and between 1238 and 1319 °C, forming a trend that fits the geotherm adiabat curve of an ascending asthenospheric mantle (Figure 7).

5. Discussion

5.1. Primary Poorly Depleted Spinel-Facies Mantle Column beneath Huanul Volcano

The mineralogical association suggests that Huanul xenoliths have been equilibrated in the spinel-facies stability field. Accordingly, the calculated P of equilibration ranges between 10 and 25 kbar. No evidence of a deeper provenance such as garnet breakdown or garnet relics was found.

The mineral modal composition (i.e., spinel-facies lherzolites; Figure 3) coupled with major and trace elements composition of the mineral phases (Figures 5 and 6) suggest that melting and metasomatic processes did not affect or only slightly affected the spinel-facies mantle column in this region. A similar hypothesis was suggested for xenoliths from Agua Poca volcano (also located in Payenia) [10], which also show similar major elements minerals composition with the exception of the spongy clinopyroxenes (Figure 5). Noticeably, a group of xenoliths from Agua Poca have spinels with high Cr# and low Mg#, similar to our reacted spinels. However, no reaction textures were reported for Agua Poca xenoliths.

Conversely, metasomatic and depletion processes are instead widely recorded by xenoliths from the entire Patagonia (e.g., [7,9,11–14,16–19] and references therein).

Clinopyroxene REE patterns are consistent with residues after 1 to 3% of nonmodal partial melting of a PM composition (Figure 6). Similar degrees of partial melting have been obtained using different equations based on spinel Cr# (i.e., [61–63]), with F (%) values mainly between 0 and 4% (Figure 8; Table 3) and by OSMA diagram ([64]). As expected, a direct relationship between F% and olivine content is recognized.

Table 3. Calculated T (°C), P (kbar) and F (%) of Huanul xenoliths. Geothermometers: (1) Wells [52]; (2) two-pyroxene, Brey and Kohler [54]; (3) Ca in Opx, Brey and Kohler [54]; (4) Taylor [55]; (5) Nimis and Grutter [56]; (7) Equation 2 from Wang et al. [58]; (9) Equation 32d from Putirka [59]. Geobarometer: (6) Mercier [53]; (8) Equation 1 from Wang et al. [58]; (10) Equation 32a from Putirka [59]. Degree of melting (F): (11) Batanova et al. [61]; (12) Hellebrand et al. [62]; (13) Warren [63].

Sample		Primary						Spongy				Spinels		
		1	2	3	4	5	6	7	8	9	10	11	12	13
		T	T	T	T	T	P	T	P	T	P	F	F	F
HU11	Avg.	929	969	904	908	905	19					5.6	3.2	4.3
	Min	885	908	884	848	886	17					5.4	3.0	4.1
	Max	960	1021	937	947	939	22					5.8	3.4	4.5
HU12	Avg.	1029	1107	918	920	1052	24	1263	8.0	1260	9.4	4.1	1.7	2.9
	Min	1021	1103	908	910	1043	24	1260	7.9	1259	9.2	3.8	1.4	2.6
	Max	1035	1117	926	927	1058	25	1265	8.2	1260	9.6	4.4	2.0	3.2
HU14	Avg.	1108	1175	1185	1168	1151	22	1239	6.4	1256	8.8	9.7	7.4	8.1
	Min	1059	1089	1156	1102	1129	20	1238	6.3	1245	7.9	9.6	7.3	8.0
	Max	1138	1222	1204	1211	1166	24	1240	6.5	1265	9.4	9.8	7.6	8.2
HU15	Avg.							1289	9.6	1252	9.3	4.5	2.0	3.2
	Min							1279	9.1	1237	8.3	4.4	2.0	3.2
	Max							1306	10.0	1264	10.3	4.5	2.1	3.3
HU19	Avg.	950	979	940	941	942	20					2.8	0.3	1.7
	Min	935	959	936	916	938	20					2.6	0.2	1.5
	Max	961	999	944	961	946	21					3.1	0.6	1.9
HU20	Avg.	942	969	921	929	923	22					4.0	1.6	2.8
	Min	920	948	910	898	912	20					3.0	0.5	1.9
	Max	978	1007	934	978	935	23					6.4	4.0	5.0
HU21	Avg.	951	980	953	947	953	20					4.0	1.5	2.8
	Min	934	958	912	923	914	18					3.8	1.3	2.6
	Max	964	993	984	972	983	23					4.2	1.7	3.0
HU22	Avg.	932	966	944	918	945	20					2.9	0.4	1.8
	Min	918	950	920	892	922	18					2.4	-0.1	1.3

	Max	946	984	977	940	976	21					3.5	1.0	2.3
	Avg.							1296	12.5	1339	17.5	10.3	8.1	8.7
HU23	Min							1278	11.2	1323	15.8	10.2	7.9	8.5
	Max							1319	14.0	1358	19.4	10.6	8.3	8.9
	Avg.							1308	11.3	1296	13.0	8.6	6.3	7.0
HU25	Min							1294	11.0	1261	10.7	8.4	6.1	6.9
	Max							1318	11.7	1316	14.3	8.7	6.4	7.1
	Avg.	887	914	881	848	883	16					2.3	0.2	1.3
HU32	Min	880	903	875	837	877	15					2.2	-0.2	1.1
	Max	893	925	887	858	889	18					2.6	0.3	1.5
	Avg.	849	852	832	781	831	13					3.2	0.7	2.0
HU33	Min	836	814	826	752	825	10					2.9	0.4	1.8
	Max	862	890	837	809	837	15					3.4	0.9	2.2
	Avg.	976	1038	967	987	966	22					3.3	0.9	2.2
HU34	Min	960	1026	918	963	920	21					3.2	0.7	2.0
	Max	992	1050	1016	1010	1013	22					3.6	1.2	2.4

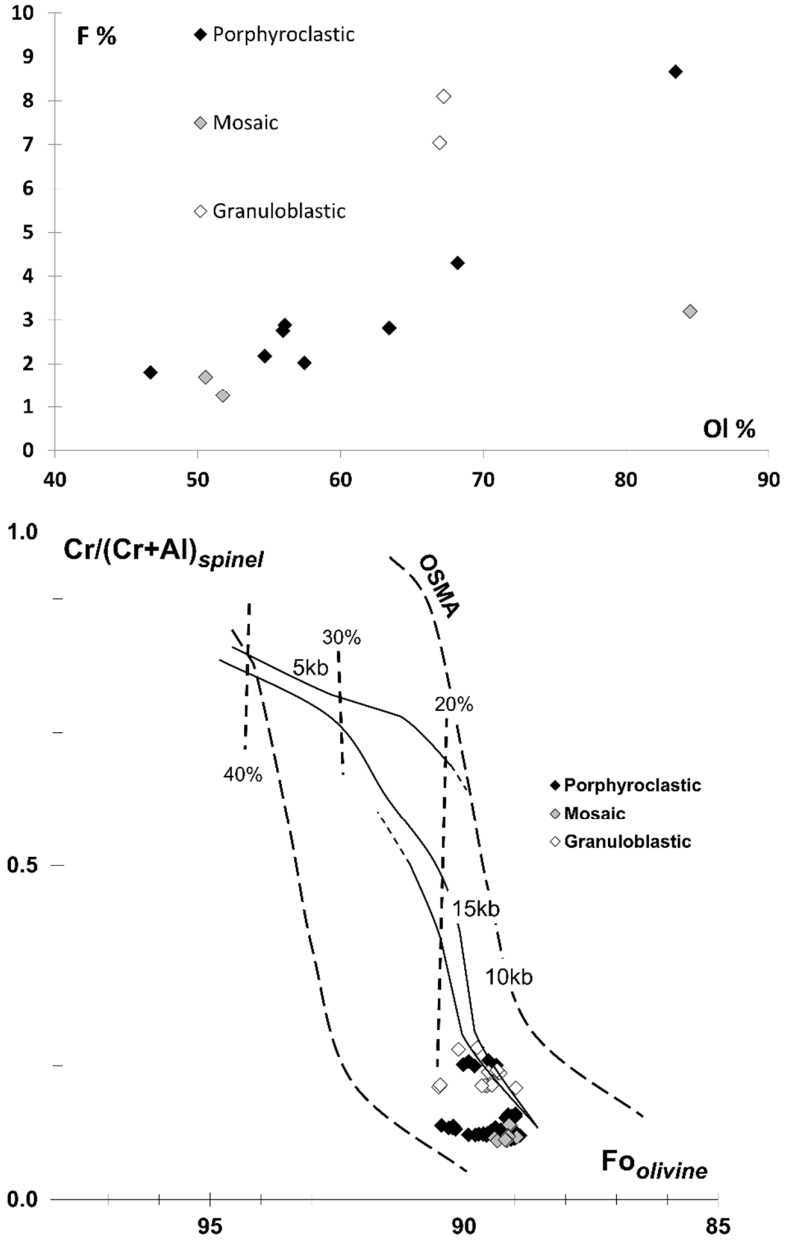

Figure 8. F% estimated with the equation of Warren [63] vs. Olivine modal abundance; OSMA diagram from Arai [64]: Cr/(Cr + Al) in spinel vs Fosterite content in olivine.

Temperatures estimated for the spinel-facies Huanul xenoliths are lower compared to other Patagonian localities, in agreement with a colder mantle column that underwent low degrees of partial melting (Figure 7). Noticeably, Huanul xenoliths mainly plot along a geotherm colder than Agua Poca. However, granuloblastic sample HU14 follows a trend similar to Agua Poca (Figure 7), thus suggesting that the granuloblastic texture could be related to localized heating of the mantle column. This is also in agreement with degrees of melting up to 13% estimated for Agua Poca [10].

Calculated melts in equilibrium with the LREE-depleted xenoliths have a MORB-like geochemical affinity (Figure 9), different from the host basalt HU06.

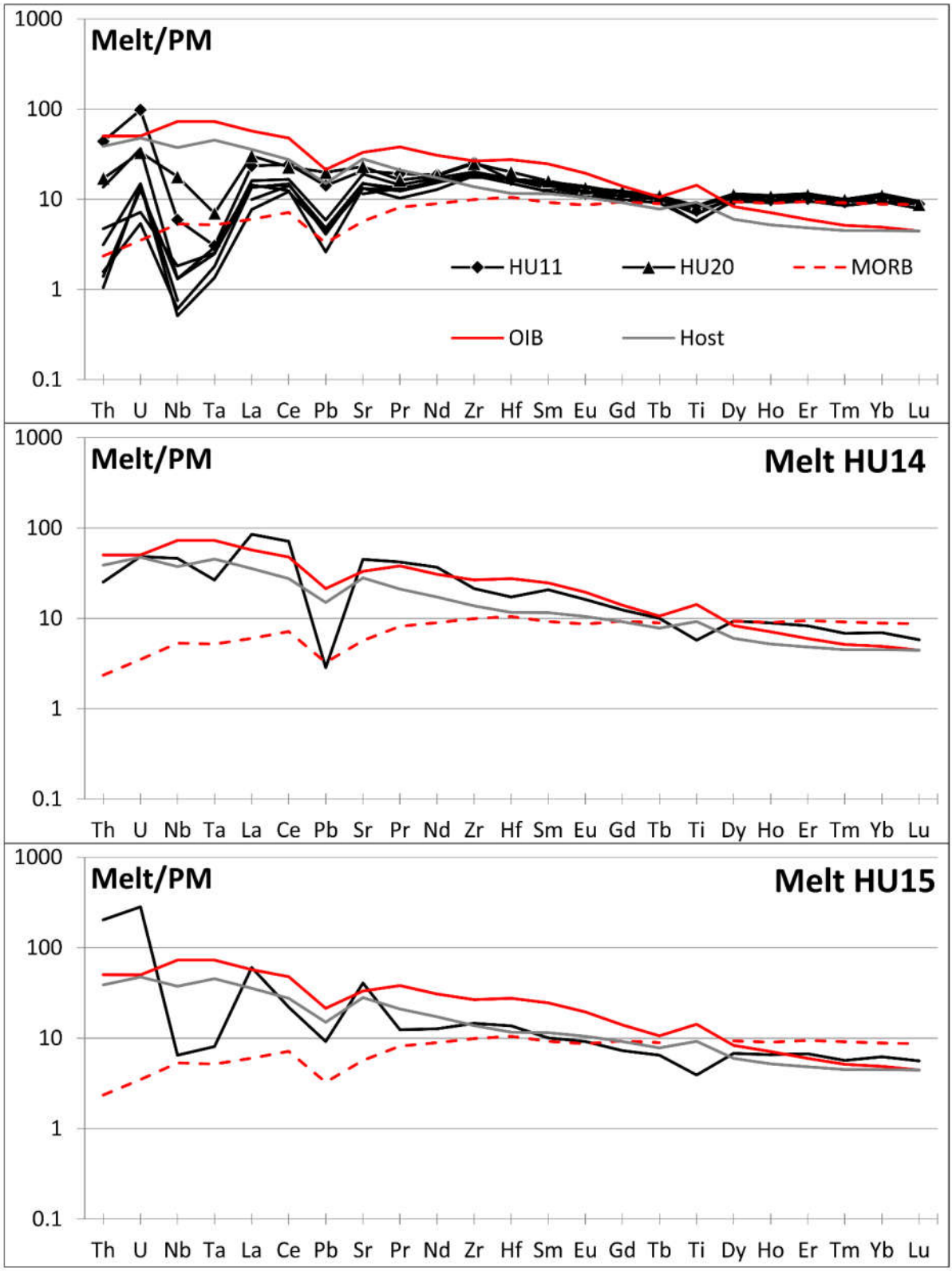

Figure 9. Spiderdiagrams of melts in equilibrium with clinopyroxene calculated using the partition coefficients of Ionov et al. [51]. Values are normalized to Primitive Mantle (PM) values from McDonough and Sun [48].

This suggests that the source of the Huanul magmatism was deeper than 25 kbar, possibly in the asthenosphere. The steeper T-P trend of Huanul and Agua Poca xenoliths compared to common geotherms of the subcontinental lithospheric mantle indicates possible melt upwelling pathways from the asthenosphere (Figure 7). This is also in agreement with the spongy clinopyroxene estimations which fit the modeled adiabat curve.

This evidence also suggests that the slight depletion of the mantle column was an inherited feature and was not induced by percolation of the host basalt melt. According to Chilson-Parks et al. [20], part of the Payenia basalts derive from an asthenospheric source with geochemical affinities to the Discovery-Shona MORB source. Based on major and trace element abundances and isotope ratios of the Payenia basalts, they suggest that the Payenia SCLM was twice metasomatized 50 to 150 Ma. One melt was generated from the Discovery-Shona MORB source, while the second one derived from the mantle-wedge during subduction of the Pacific plate. In this framework, the primary composition of our xenoliths could represent the source of this magmatism with MORB-affinity. Regional geophysical [65] and geodynamic [66] studies of the Payenia region have revealed a low seismic velocity structure in the region down to 200 km, indicative of upwelling of deep, hot asthenospheric material. This Neogene structure has been related either to the steepening of the subducted Nazca plate [65] or to the subduction of the hypothetical 'Payenia' mantle plume [66]. On this basis, the primary texture and mineralogical and geochemical features of our xenoliths might have recorded the original characteristics of the subcontinental lithospheric mantle prior to the Neogene asthenospheric upwelling, while the spongy and reaction textures might reflect the latest interaction with the upwelling mantle.

5.2. Xenolith-Melt Interaction during Magma Ascent

The majority of Huanul xenoliths do not show chemical evidences of refertilization or melt/rock interaction processes. However, two main reactions are recognized in the mineral textures of HUA14 and HUA15 samples mainly affecting clinopyroxene and spinel phases. The first one is testified by the replacement of exsoluted clinopyroxene by spongy clinopyroxene (Figure 4G,I). The second reaction produced recrystallization of spinel and formation of reacted spinel structures (Figure 4I). In both cases, neoblasts of olivine and plagioclase in a fine matrix (in spinel reaction) or as inclusions (in spongy-clinopyroxene) are part of the new mineralogical association. The occurrence of plagioclase as stable phase in the reactions supports a shallow depth for the melt–xenolith interaction, thus suggesting that the migrating melt could be related to the host basalt and that the interaction occurred during the ascent of the xenolith. This hypothesis is also supported by the fact that these structures occur in crystals in contact with veins, which in turn are connected with the host basalt. Further evidence is the occurrence of olivine neoblasts within the recrystallization zone with Mg# values lower than those accepted for mantle olivine (Mg# = 77.5 − 65.1), thus possibly derived from direct crystallization of the migrating melt. The direct crystallization of olivine neoblasts together with the resorption of orthopyroxene, as testified by lobate shapes of orthopyroxenes at the contact with the host basalt, suggests that the migrating melt was Si-poor, thus consistent with the host basalt HU06 [41]. In addition, the trace element composition of partial and complete spongy clinopyroxenes (samples HU14 and HU15) is more enriched in Ba, Nb and Ta compared to the other xenoliths (Figure 6). In particular, partially spongy clinopyroxene cores from sample HU15 show enrichments in LREE comparable with chromatographic effects related to melt-rock reaction processes as observed in other Patagonian mantle xenoliths (e.g., [11,14]) and in the Fernando de Noronha xenoliths (Figure 10b,c of Rivalenti et al. [67]). Conversely, the convex-upward REE patterns of HU14 spongy clinopyroxenes are commonly interpreted as evidence of a prolonged interaction with an alkaline melt (e.g., [11]). Thus, these spongy clinopyroxenes can provide constrains on the composition of the percolating melt. Calculated melts in equilibrium with these

clinopyroxenes using the coefficients of Ionov et al. [51] are similar to the host basalt HU06 (Figure 9), thus suggesting infiltration of the host basalt.

Spongy-textures are widely known in mantle xenoliths, and their origin has been attributed to (1) metasomatic processes before contact with the host magma (e.g., [68]), (2) to host magma-xenoliths interactions (e.g., [69]), or (3) to partial melting induced by decompression (e.g., [70]). Huanul secondary spinels related to reaction textures have been produced by higher degree of melting compared to primary spinels (F of 3.9–8.7% and 1.1–4.5%, respectively) and their associated spongy clinopyroxenes are characterized by lower HREE content compatible with more depleted PM compositions (i.e., 5% and 1–3% PM melting degrees, respectively). The melt-crystal reaction has also shifted the mineral composition toward more restitic terms: reacted spinels are enriched in Cr_2O_3 (8.50–12.46 and 11.62–20.47 wt.% in primary and reacted spinels, respectively) and FeO (8.95–12.02 and 10.31–13.31 wt.%) while depleted in Al_2O_3 (56.64–60.43 and 46.75–57.47 wt.%) and MgO (18.83–21.79 and 17.79–20.41 wt.%). Spongy clinopyroxenes show depletion in Na_2O (1.06–2.18 and 0.35–0.96 wt.% for primary and spongy clinopyroxenes, respectively) and Al_2O_3 (5.51–9.64 and 3.98–6.78 wt.%) and are enriched in FeO (13.26–16.00 and 16.33–17.69 wt.%). The occurrence of spongy and reaction textures at the contact with basaltic veins or the host basalt suggests that these structures in Huanul xenoliths are related to the percolation of the host basalt and interaction of the melt with the mineral phases.

6. Conclusions

This is the first petrographic and geochemical study of mantle xenoliths entrained in the lava flows of the Huanul shield volcano. We found evidences of a poorly-depleted, almost primitive subcontinental lithospheric mantle beneath the southern Payenia Volcanic Province. This is a rare occurrence among the many xenoliths collected from Argentina and Patagonia, where mantle xenoliths record multiple events of depletion and refertilization related to the Pacific subduction below South America. The Huanul xenoliths' geochemical and mineralogical features are similar to those of xenoliths from the Agua Poca volcano, a close locality that, however, has recorded higher degrees of partial melting.

Xenoliths in Huanul volcano are lherzolitic in composition and equilibrated in the spinel-facies between 10 and 25 kbar (~33–79 km). They mainly fall on a 50–60 mW/m^2 geotherm, with T increasing from 814 to 1170 °C, steeper than geotherm models for subcontinental lithospheric mantle. Interaction of the xenoliths with the host basalt during ascent is recorded by the formation of spongy textures in clinopyroxene and reacted spinel in contact with basalt veins or the host basalt. In these textures, the primary minerals are recrystallized toward more refractory compositions accompanied by segregation of plagioclase and olivine, which document a relatively shallow depth between 6–14 kbar for the melt-rock interaction event. The extremely high T estimations for spongy clinopyroxene follow the adiabat curve of subcontinental lithospheric mantle and are in good agreement with chemical evidences of interaction with the alkaline host lava.

Taken together our data indicate that this xenolith population of Huanul could represent the Discovery-Shona asthenospheric MORB source invoked by Chilson-Parks et al. [20] for the magmatism of the southern Payenia region. In addition, Huanul xenoliths do not show any evidence of a SCLM pertaining to a mantle wedge domain metasomatized by the subducting slab, thus making the Payenia Volcanic Province a unique and important location to investigate the primitive geochemical character of the SCLM of South America.

Supplementary Materials: The following supporting information can be downloaded at: www.mdpi.com/article/10.3390/geosciences12040157/s1, Table S1: Major element concentrations of minerals from the Huanul mantle xenoliths; Table S2: Clinopyroxene trace element concentrations from Huanul mantle xenoliths.

Author Contributions: Investigation, G.W.B., M.M., T.G., R.V.C., A.Z., M.E.S., M.I.B., A.D.P., T.J., F.G. and A.C. Writing—review and editing T.G., M.M., A.C. and G.W.B. All authors have read and agreed to the published version of the manuscript.

Funding: Programmi di Ricerca di Interesse Nazionale of the Italian Ministero dell'Istruzione, dell'Università e della Ricerca (protocol 20178LPCPW), Facultad de Ciencias Exactas y Naturales-PI3-12G (Universidad Nacional de La Pampa, Argentina), CNR–CONICET joint programme.

Data Availability Statement: The data presented in this study are available in this article and its Supplementary Materials Tables S1 and S2.

Acknowledgments: We thank two anonymous reviewers whose suggestions helped to improve the manuscript. All the Editor staff is also acknowledged.

Conflicts of Interest: The authors declare no conflict of interest.

References

1. Barbieri, M.A.; Rivalenti, G.; Cingolani, C.; Vanucci, R.; Kempton, P. Geochemical and isotope constraints on the composition of the mantle lithosphere in Patagonia (Argentina, Chile). In *Actas of Second South American Symposium on Isotope Geology*; Servicio Geologico Minero Argentino: Carlos Paz, Argentina, 1999; Volume 2, pp. 163–166, ISSN 0328-2325.
2. Bertotto, G.W. Cerro Agua Poca, un cono basáltico cuaternario portador de xenolitos ultramáficos, en el oeste de la provincia de La Pampa, Argentina. *Rev. Asoc. Geol. Argent.* **2000**, *55*, 59–71.
3. Rivalenti, G.; Mazzuchelli, M.; Laurora, A.; Ciuffi, S.; Zanetti, A.; Vannucci, R.; Cingolani, C.A. The back arc mantle lithosphere in Patagonia, South America. *J. S. Am. Earth Sci.* **2004**, *17*, 121–152. https://doi.org/10.1016/j.jsames.2004.05.009.
4. Bjerg, E.A.; Ntaflos, T.; Kurat, G.; Dobosi, G.; Labudia, C. The upper mantle beneath Patagonia, Argentina, documented by xenoliths from alkali basalts. *J. S. Am. Earth Sci.* **2005**, *18*, 125–145. https://doi.org/10.1016/j.jsames.2004.09.002.
5. Schilling, M.E.; Carlson, R.W.; Conceição, R.V.; Dantas, C.; Bertotto, G.W.; Koester, E. Re–Os isotope constraints on subcontinental lithospheric mantle evolution of southern South America. *Earth Planet. Sci. Lett.* **2008**, *268*, 89–101. https://doi.org/10.1016/j.epsl.2008.01.005.
6. Schilling, M.A.; Carlson, R.W.; Tassara, A.; Conceição, R.V.; Bertotto, G.W.; Vásquez, M.; Muñoz, D.; Jalowitzki, T.; Gervasoni, F.; Morata, D. The origin of Patagonia revealed by Re-Os systematics of mantle xenoliths. *Precambrian Res.* **2017**, *294*, 15–32. https://doi.org/10.1016/j.precamres.2017.03.008.
7. Jalowitzki, T.L.R.; Conceiçao, R.V.; Orihashi, Y.; Bertotto, G.W.; Nakai, S.; Schilling, M. Evoluçao geoquímica de Peridotitos e Piroxenitos do Manto Litosférico Subcontinental do vulcão Agua Poca, Terreno Cuyania, Argentina. *Pesqui. Geociências* **2010**, *37*, 143–167.
8. Jalowitzki, T.; Sumino, H.; Conceição, R.V.; Orihashi, Y.; Nagao, K.; Bertotto, G.W.; Balbinot, E.; Schilling, M.E.; Gervasoni, F. Noble gas composition of subcontinental lithospheric mantle: An extensively degassed reservoir beneath Southern Patagonia. *Earth Planet. Sci. Lett.* **2016**, *450*, 263–273. https://doi.org/10.1016/j.epsl.2016.06.034.
9. Jalowitzki, T.; Gervasoni, F.; Conceição, R.V.; Orihashi, Y.; Bertotto, G.W.; Sumino, H.; Schilling, M.E.; Nagao, K.; Morata, D.; Sylvester, P. Slab-derived components in the subcontinental lithospheric mantle beneath Chilean Patagonia: Geochemistry and Sr–Nd–Pb isotopes of mantle xenoliths and host basalt. *Lithos* **2017**, *292–293*, 179–197. https://doi.org/10.1016/j.lithos.2017.09.008.
10. Bertotto, G.W.; Mazzucchelli, M.; Zanetti, A.; Vannucci, R. Petrology and geochemistry of the back-arc lithospheric mantle beneath eastern Payunia (La Pampa, Argentina): Evidence from Agua Poca peridotite xenoliths. *Geochem. J.* **2013**, *47*, 219–234.
11. Bertotto, G.W.; Mazzucchelli, M.; Zanetti, A.; Ponce, A.D.; Giovanardi, T.; Brunelli, D.; Bernardi, M.I.; Hémond, C.; Cipriani, A. Mantle heterogeneities produced by open-system melting and melt/rock reactions in Patagonian extra-Andean backarc mantle (Paso de Indios, Argentina). *J. S. Am. Earth Sci.* **2021**, *106*, 103002.
12. Ponce, A.; Bertotto, G.W.; Zanetti, A.; Brunelli, D.; Giovanardi, T.; Aragón, E.; Bernardi, M.; Hémond, C.; Mazzucchelli, M. Short-scale variability of the SCLM beneath the extra-Andean back arc (Paso de Indios, Argentina): Evidence from spinel-facies mantle xenoliths. *Open Geosci.* **2015**, *7*, 362–385. https://doi.org/10.1515/geo-2015-0023.
13. Mazzucchelli, M.; Cipriani, A.; Hémond, C.; Zanetti, A.; Bertotto, G.W.; Cingolani, C.A. Origin of the DUPAL anomaly in mantle xenoliths of Patagonia (Argentina) and geodynamic consequences. *Lithos* **2016**, *248–251*, 257–271. https://doi.org/10.1016/j.lithos.2016.01.010.
14. Melchiorre, M.; Faccini, B.; Grégoire, M.; Benoit, M.; Casetta, F.; Coltorti, M. Melting and metasomatism/refertilisation processes in the Patagonian sub-continental lithospheric mantle: A review. *Lithos* **2020**, *354–355*, 105324. https://doi.org/10.1016/j.lithos.2019.105324.
15. Novais-Rodrigues, E.; Jalowitzki, T.; Gervasoni, F.; Sumino, H.; Bussweiler, Y.; Klemme, S.; Berndt, J.; Conceição, R.V.; Schilling, M.E.; Bertotto, G.W.; et al. Partial melting and subduction-related metasomatism recorded by geochemical and isotope (He-Ne-Ar-Sr-Nd) compositions of spinel lherzolite xenoliths from Coyhaique, Chilean Patagonia. *Gondwana Res.* **2021**, *98*, 257–276. https://doi.org/10.1016/j.gr.2021.06.003.
16. Kilian, R.; Stern, C.R. Constraints on the interaction between slab melts and the mantle wedge from adakitic glass in peridotite xenoliths. *Eur. J. Mineral.* **2002**, *14*, 25–36. https://doi.org/10.1127/0935-1221/2002/0014-0025.

17. Ntaflos, T.; Bjerg, E.A.; Labudia, C.H.; Kurat, G. Depleted lithosphere from the mantle wedge beneath Tres Lagos, southern Patagonia, Argentina. *Lithos* **2007**, *94*, 46–65. https://doi.org/10.1016/j.lithos.2006.06.011.
18. Gervasoni, F.; Conceição, R.V.; Jalowitzki, T.L.R.; Schilling, M.E.; Orihashi, Y.; Nakai, S.; Sylvester, P. Heterogeneidades do manto litosférico subcontinental no extremo sul da Placa Sul-americana: Influência da subducção atual e interações litosfera-astenosfera sob o Campo Vulcânico de Pali Aike. *Pesqui. Geocienc.* **2012**, *39*, 269–285.
19. Faccini, B.; Bonadiman, C.; Coltorti, M.; Gregoire, M.; Siena, F. Oceanic material recycled within the Sub-Patagonian Lithospheric Mantle (Cerro del Fraile, Argentina). *J. Petrol.* **2013**, *6*, 1211–1258. https://doi.org/10.1093/petrology/egt010.
20. Chilson-Parks, B.H.; Calabozo, F.M.; Saal, A.E.; Wang, Z.; Mallick, S.; Petrinovic, I.A.; Frey, F.A. The signature of metasomatized subcontinental lithospheric mantle in the basaltic magmatism of the Payenia volcanic province, Argentina. *Geochem. Geophys. Geosyst.* **2022**, *23*, e2021GC010071. https://doi.org/10.1029/2021GC010071.
21. Bernardi, M.I.; Bertotto, G.W.; Jalowitzki, T.R.L.; Orihashi, Y.; Ponce, A.D. Emplacement history and inflation evidence of a long basaltic lava flow located in Southern Payenia Volcanic Province, Argentina. *J. Volcanol. Geotherm. Res.* **2015**, *293*, 46–56.
22. Cobbold, P.R.; Rossello, E.A. Aptian to recent compressional deformation, foothills of the Neuquén Basin, Argentina. *Mar. Pet. Geol.* **2003**, *20*, 429–443. https://doi.org/10.1016/S0264-8172(03)00077-1.
23. Kay, S.M.; Burns, W.M.; Copeland, P.; Mancilla, O. Upper Cretaceous to Holocene magmatism and evidence for transient Miocene shallowing of the Andean subduction zone under the northern Neuquén Basin. In *Evolution of an Andean Margin: A Tectonic and Magmatic View from the Andes to the Neuquén Basin (35–39° S Lat.)*; Kay, S.M., Ramos, V.A., Eds.; Special Paper; Geological Society of America: Boulder, CO, USA, 2006; Volume 407, pp. 67–96.
24. Galland, O.; Hallot, E.; Cobbold, P.R.; Buffet, G. Volcanismin a compressional Andean setting: A structural and geochronological study of Tromen volcano (Neuquen Province, Argentina). *Tectonics* **2007**, *26*, TC4010. https://doi.org/10.1029/2006TC002011.
25. Folguera, A.; Naranjo, J.A.; Orihashi, Y.; Sumino, H.; Nagao, K.; Polanco, E.; Ramos, V.A. Retroarc volcanism in the northern San Rafael block (34–35°30′ S), southern Central Andes: Occurrence, age, and tectonic setting. *J. Volcanol. Geotherm. Res.* **2009**, *186*, 169–185.
26. Quidelleur, X.; Carlut, J.; Tchilinguirian, P.; Germa, A.; Gillot, P.Y. Paleomagnetic directions from mid-latitude sites in the southern hemisphere (Argentina): Contribution to time averaged field models. *Phys. Earth Planet. Inter.* **2009**, *172*, 199–209. https://doi.org/10.1016/j.pepi.2008.09.012.
27. Germa, A.; Quidelleur, X.; Gillot, P.Y.; Tchilinguirian, P. Volcanic evolution of the back-arc Pleistocene Payun Matru volcanic field (Argentina). *J. S. Am. Earth Sci.* **2010**, *29*, 717–730. https://doi.org/10.1016/j.jsames.2010.01.002.
28. Gudnason, J.; Holm, P.M.; Søager, N.; Llambías, E.J. Geochronology of the late Pliocene to recent volcanic activity in the Payenia back-arc volcanic province, Mendoza Argentina. *J. S. Ameraican Earth Sci.* **2012**, *37*, 191–201. https://doi.org/10.1016/j.jsames.2012.02.003.
29. Ramos, V.A.; Folguera, A. Tectonic evolution of the Andes of Neuquén: Constraints derived from the magmatic arc and foreland deformation. In *The Neuquén Basin: A Case Study in Sequence Stratigraphy and Basin Dynamics*; Veiga, G., Spalletti, L.A., Howell, J.A., Eds.; Special Publication; Geological Society: Boulder, CO, USA, 2005; Volume 252, pp. 15–35.
30. Ramos, V.A.; Kay, S.M. Overview of the tectonic evolution of the Southern Central Andes of Mendoza and Neuquén (35–39° S latitude). In *Evolution of an Andean Margin: A Tectonic and Magmatic View from the Andes to the Neuquén Basin (35–39° S)*; Kay, S.M., Ramos, V.A., Eds.; Special Publication; Geological Society of America: Boulder, CO, USA, 2006; Volume 407, pp. 1–18.
31. Bermúdez, A.; Delpino, D.; Frey, F.; Saal, A. Los basaltos de retroarco extraandinos. In *Geología y Recursos Naturales de Mendoza, Relatorio. XII Congreso Geológico Argentino y II Congreso de Exploración de Hidrocarburos*; Ramos, V.A., Ed.; Asociación Geológica: Buenos Aires, Argentina, 1993; pp. 161–173.
32. James, D.E.; Sacks, I.S. Cenozoic formation of the Central Andes: A geophysical perspective. In *Geology and Ore Deposits of the Central Andes*; Skinner, B.J., Ed.; Special Publication; Society of Economic Geologists: Littleton, CO, USA, 1999; Volume 7, pp. 1–26.
33. Kay, S.M.; Gorring, M.; Ramos, V. Magmatic sources, setting and causes of Eocene to recent Patagonian plateau magmatism (36° S to 52° S latitude). *Rev. Asoc. Geol. Argent.* **2004**, *59*, 556–568.
34. Kay, S.M.; Godoy, E.; Kurtz, A. Episodic arcmigration, crustal thickening, subduction erosion, and magmatism in the south-central Andes. *Geol. Soc. Am. Bull.* **2005**, *117*, 67–88. https://doi.org/10.1130/B25431.1.
35. Bernardi, M.I.; Bertotto, G.W.; Ponce, A.D.; Orihashi, Y.; Sumino, H. Volcanology and inflation structures of an extensive basaltic lava flow in the Payenia Volcanic Province, extra-Andean back arc of Argentina. *Andean Geol.* **2019**, *46*, 279–299.
36. Mazzarini, F.; Fornaciai, A.; Bistacchi, A.; Pasquarè, F.A. Fissural volcanism, polygenetic volcanic fields, and crustal thickness in the Payen Volcanic Complex on the central Andes foreland (Mendoza, Argentina). *Geochem. Geophys. Geosyst.* **2008**, *9*, Q09002.
37. Risso, C.; Németh, K.; Combina, A.M.; Nullo, F.; Drosina, M. The role of phreatomagmatism in a Plio–Pleistocene high-density scoria cone field: Llancanelo Volcanic Field (Mendoza), Argentina. *J. Volcanol. Geotherm. Res.* **2008**, *169*, 61–86. https://doi.org/10.1016/j.jvolgeores.2007.08.007.
38. Inbar, M.; Risso, C. A morphological and morphometric analysis of a high density cinder cone volcanic field-Payun Matru, south-central Andes, Argentina. *Z. Geomorphol.* **2001**, *45*, 321–343.
39. Bertotto, G.W.; Bjerg, E.A.; Cingolani, C.A. Hawaiian and Strombolian style monogenetic volcanism in the extra-Andean domain of central-west Argentina. *J. Volcanol. Geotherm. Res.* **2006**, *158*, 430–444. https://doi.org/10.1016/j.jvolgeores.2006.08.00.

40. Bertotto, G.W.; Orihashi, Y.; Nagao, K.; Motoki, A. New K-Ar ages on retroarc basalts of Mendoza-La Pampa. In Proceedings of the Segundo Encuentro Científico del ICES, Buenos Aires, Argentina, 28–31 November 2006.
41. Bertotto, G.W.; Cingolani, C.A.; Bjerg, E.A. Geochemical variations in Cenozoic back-arc basalts at the border of La Pampa and Mendoza provinces, Argentina. *J. S. Am. Earth Sci.* **2009**, *28*, 360–373.
42. Bernardi, M.I. Petrología y Volcanología de los Flujos Basálticos Neógeno-Cuaternarios del Retroarco Extraandino Entre los 36° y 37°30′LS, Provincias de Mendoza y La Pampa, Argentina. Ph.D. Thesis, Universidad Nacional de Córdoba, Córdoba, Argentina, 2016; 353p.
43. Stern, C.R.; Frey, F.A.; Futa, K.; Zartman, R.E.; Peng, Z.; Kyser, K.T. Trace-element and Sr, Nd, Pb, and O isotopic composition of Pliocene and Quaternary alkali basalts of the Patagonian Plateau lavas of southernmost South America. *Contrib. Mineral. Petrol.* **1990**, *104*, 294–308. https://doi.org/10.1007/BF00321486.
44. Giovanardi, T.; Zanetti, A.; Dallai, L.; Morishita, T.; Hémond, C.; Mazzucchelli, M. Evidence of subduction-related components in sapphirine-bearing gabbroic dykes (Finero phlogopite–peridotite): Insights into the source of the Triassic–Jurassic magmatism at the Europe–Africa boundary. *Lithos* **2020**, *356–357*, 105366. https://doi.org/10.1016/j.lithos.2020.105366.
45. Giovanardi, T.; Mazzucchelli, M.; Zanetti, A.; Langone, A.; Tiepolo, M.; Cipriani, A. Occurrence of phlogopite in the finero mafic layered complex. *Cent. Eur. J. Geosci.* **2014**, *6*, 588–613.
46. Harte, B. Rock nomenclature with particular relation to deformation and recrystallization textures in olivine bearing xenoliths. *J. Geol.* **1977**, *85*, 279–288.
47. Lyubetskaya, T.; Korenaga, J. Chemical composition of Earth's primitive mantle and its variance: 1. Method and results. *J. Geophys. Res.* **2007**, *112*, B03211.
48. McDonough, W.F.; Sun, S. The composition of the Earth. *Chem. Geol.* **1995**, *120*, 223–253. https://doi.org/10.1016/0009-2541(94)00140-4.
49. Sun, S.; McDonough, W.F. Chemical and isotopic systematics of oceanic basalts; implications for mantle composition and processes. In *Magmatism in the Ocean Basins*; Saunders, A., Norry, M., Eds.; Special Publication; Geological Society: Boulder, CO, USA, 1989; Volume 42, pp. 313–345. https://doi.org/10.1144/GSL.SP.1989.042.01.19.
50. Hofmann, A.W. Chemical differentiation of the Earth: The relationship between mantle, continental crust and oceanic crust. *Earth Planet. Sci. Lett.* **1988**, *90*, 297–314.
51. Ionov, D.A.; Bodinier, J.L.; Mukasa, S.B.; Zanetti, A. Mechanisms and sources of mantle metasomatism: Major and trace element compositions of peridotite xenoliths from Spitsbergen in the context of numerical modelling. *J. Petrol.* **2002**, *43*, 2219–2259.
52. Wells, P.R. Pyroxene thermometry in simple and complex systems. *Contrib. Mineral. Petrol.* **1977**, *62*, 129–140.
53. Mercier, J.-C.C. Single-pyroxene thermobarometry. *Tectonophysics* **1980**, *70*, 1–37. https://doi.org/10.1016/0040-1951(80)90019-0.
54. Brey, G.; Köhler, T. Geothermobarometry in four-phase lherzolites II. New thermobarometers, and practical assessment of existing thermobarometers. *J. Petrol.* **1990**, *31*, 1353–1378. https://doi.org/10.1093/petrology/31.6.1353.
55. Taylor, W.R. An experimental test of some geothermometer and geobarometer formulations for upper mantle peridotites with application to the thermobarometry of fertile lherzolite and garnet websterite. *Neues Jahrb. Mineral. Abh.* **1998**, *172*, 381–408. https://doi.org/10.1127/njma/172/1998/381.
56. Nimis, P.; Grütter, H. Internally consistent geothermometers for garnet peridotites and pyroxenites. *Contrib. Mineral. Petrol.* **2010**, *159*, 411–427.
57. Yang, H.-J.; Frey, F.A.; Weis, D.; Giret, A.; Pyle, D.; Michon, G. Petrogenesis of the Flood Basalts Forming the Northern Kerguelen Archipelago: Implications for the Kerguelen Plume. *J. Petrol.* **1998**, *39*, 711–748.
58. Wang, X.; Hou, T.; Wang, M.; Zhang, C.; Zhang, Z.; Pan, R.; Marxer, F.; Zhang, H. A new clinopyroxene thermobarometer for mafic to intermediate magmatic systems. *Eur. J. Mineral.* **2021**, *33*, 621–637. https://doi.org/10.5194/ejm-33-621-2021.
59. Putirka, K.D. Thermometers and Barometers for Volcanic Systems. *Rev. Mineral. Geochem.* **2008**, *69*, 61–120.
60. Hasterok, D.; Chapman, D. Heat production and geotherms for the continental lithosphere. *Earth Planet. Sci. Lett.* **2011**, *307*, 59–70.
61. Batanova, V.G.; Suhr, G.; Sobolev, V. Origin of geochemical heterogeneity in the mantle peridotites from the Bay of Islands ophiolite, Newfoundland, Canada: Ion probe study of clinopyroxenes. *Geochim. Cosmochim. Acta* **1998**, *62*, 853–866.
62. Hellebrand, E.; Snow, J.E.; Dick, H.J.B.; Hofmann, A.W. Coupled major and trace elements as indicators of the extent of melting in mid-ocean-ridge peridotites. *Nature* **2001**, *410*, 677–681. https://doi.org/10.1038/35070546.
63. Warren, J.M. Global variations in abyssal peridotite compositions. *Lithos* **2016**, *248–251*, 193–219.
64. Arai, S. Characterization of spinel peridotites by olivine-spinel compositional relationships: Review and interpretation. *Chem. Geol.* **1994**, *113*, 191–204.
65. Ramos, V.A.; Folguera, A. Payenia volcanic province in the Southern Andes: An appraisal of an exceptional Quaternary tectonic setting. *J. Volcanol. Geotherm. Res.* **2011**, *201*, 53–64. https://doi.org/10.1016/j.jvolgeores.2010.09.008.
66. Gianni, G.M.; García, H.P.A.; Lupari, M.; Pesce, A.; Folguera, A. Plume overriding triggers shallow subduction and orogeny in the southern Central Andes. *Gondwana Res.* **2017**, *49*, 387–395. https://doi.org/10.1016/j.gr.2017.06.011.
67. Rivalenti, G.; Mazzucchelli, M.; Zanetti, A.; Vannucci, R.; Bollinger, C.; Hémond, C.; Bertotto, G.W. Xenoliths from Cerro de los Chenques (Patagonia): An example of slab-related metasomatism in the backarc lithospheric mantle. *Lithos* **2007**, *99*, 45–67. https://doi.org/10.1016/j.lithos.2007.05.012.

68. Bonadiman, C.; Coltorti, M.; Beccaluva, L.; Siena, F. Kimberlite-like Metasomatism and 'Garnet Signature' in Spinel-peridotite Xenoliths from Sal, Cape Verde Archipelago: Relics of a Subcontinental Mantle Domain within the Atlantic Oceanic Lithosphere? *J. Petrol.* **2005**, *46*, 2465–2493.
69. Shaw, C.S.J.; Dingwell, D.B. Experimental peridotite–melt reaction at one atmosphere: A textural and chemical study. *Contrib. Mineral. Petrol.* **2008**, *155*, 199–214.
70. Pan, S.; Zheng, J.; Yin, Z.; Griffin, W.L.; Xia, M.; Lin, A.; Zhang, H. Spongy texture in mantle clinopyroxene records decompression-induced melting. *Lithos* **2018**, *320–321*, 144–154.